Role of electron-phonon scattering on thermoelectric coefficients in pristine $Cs_2NaYbCl_6$ perovskite: A full DFT approach

Antonio Cappai,* Claudio Melis, and Luciano Colombo
Department of Physics, University of Cagliari, Cittadella Universitaria, I-09042 Monserrato (CA), Italy

(Received 27 September 2024; accepted 8 April 2025; published 20 May 2025)

Double-halide perovskites are recently attracting significant interest in the field of thermoelectric research due to the possibility of achieving very low thermal conductivity and retaining relatively high Seebeck coefficient and electrical conductivity. Accurate estimates of the transport related properties are, thus, highly desirable and are strictly linked to an extremely detailed characterization of the microscopic mechanism underlying the transport itself. To address this issue, in this study we conduct a comprehensive theoretical investigation of one of the main process-limiting carrier transports, i.e., electron-phonon scattering, in a typical double-halide perovskite, $Cs_2NaYbCl_6$. In order to quantify the specific magnitude of this process, we adopt in this study a comprehensive DFT analysis, with a focus on evaluating the resulting lifetimes (in both hole- and electron-mediated regimes), by solving iteratively the linearized Boltzmann equation. Using the evaluated lifetimes, we found distinct differences in electrical mobilities and Seebeck coefficient as a function of the temperature and carrier concentrations, revealing that the thermoelectric figure-of-merit ZT, while quite low, is significantly higher in the case of electron-mediated regime.

DOI: 10.1103/PhysRevMaterials.9.054605

I. INTRODUCTION

Double-halide perovskites (DHPs) have emerged as a highly promising class of materials, capturing an increasing interest in many fields due to their remarkable properties and versatility. These compounds are known for their ease of synthesis and manufacturing, which is crucial for scalable and cost-effective production processes [1]. Their robust chemical stability and compositional tunability further enhances their attractiveness for a variety of applications [2]. Particularly noteworthy is their ability to exhibit a wide range of electronic and optical properties, which can be finely tuned through compositional adjustments and structural modifications [3,4].

In recent years, the potential of DHPs in thermoelectric applications has been increasingly scrutinized [5–20]. In general, thermoelectric materials are characterized by their ability to convert heat into electricity and vice versa, a property quantified by the thermoelectric figure of merit ($ZT = \sigma S^2/\kappa$) [21] which depends on their electrical σ and thermal κ conductivity, as well as Seebeck coefficient S. More specifically, the electrical conductivity and Seebeck coefficient determine the material capacity to generate electric voltage in response to a temperature gradient, while the thermal conductivity affects the material ability to maintain a temperature gradient [22].

In order to maximize the ZT of DHP, great efforts are usually spent in properly selecting the chemical species of the constituent cations and anions. Due to the wide range of possible combinations deriving from the peculiar $AB_1B_2X_6$ stoichiometric formula of DHP (with A, B_1, B_2 cations and X usually a halogen), theoretical calculations in the framework of DFT are highly valuable to select the best thermoelectric candidates. This approach, however, requires care, in particular when modeling σ. Since the majority of DHP are semiconductors [23], one of the key mechanisms affecting σ is represented by the electron-phonon interaction, which by perturbing the electronic state of the system is typically discussed in terms of the electron-phonon lifetime τ_{e-ph}. As a matter of fact, the reliable determination of τ_{e-ph} requires nontrivial constitutive models [24,25] and computationally intensive calculations, often making it a bottleneck in research. This could explain why, in the exponential growing number of publications dedicated to the evaluation of thermoelectric properties of DHPs [5–8,12,13,15,17–20], the real value of σ as a function of charge carriers and temperature is seldom reported, and calculations are rather usually limited to evaluate the σ/τ_0 ratio, where an average lifetime τ_0 is guessed from experimental evidence (when available). This not only could lead to an inaccurate prediction of ZT values, but it also hinders an important aspect governing the transport phenomenon. In fact, focusing on the extremely few studies where electron-phonon scattering rates were actually calculated for DHPs [9–11], interesting insights on the mutual influence of charge carrier and phonon dynamics have been possible.

This key advancement was made possible by the use of Wannier functions, enabling efficient and accurate interpolation of electron and phonon properties over dense grids in reciprocal space [26,27]. This approach largely reduces the computational effort required to achieve high-resolution data, thus facilitating detailed and accurate modeling of electron-phonon interactions [28]. Such an accuracy has lead to the

*Contact author: acappai@dsf.unica.it

possibility to fully determine, by first-principles calculations, the electron-phonon limited mobility and conductivity by directly including the impact of electron-phonon scattering in the solution of the linearized Boltzmann transport equation, without relying on *ad hoc* assumption on the lifetime.

Within the above research scenario, here we focus on a fully *ab initio* modelisation of the charge transport coefficient of $Cs_2NaYbCl_6$ perovskite, for which we previously fully characterized the thermal transport properties [29]. Section II describes the theoretical methods used, as well as their state-of-the-art numerical implementations, focusing on structural optimization, electronic structure calculations, and electron-phonon interaction. In Sec. III, we present our results, focusing on the electron lifetimes in two different conduction regimes, namely hole-mediated and electron-mediated conduction. We provide their accurate calculation, elaborate a detailed theoretical analysis, and we show the resulting carrier mobilities. Finally, the Seebeck coefficients and the ZT values in electron- and hole-mediated regimes are estimated, revealing a very distinct difference due to the carrier lifetimes. Quantitatively, in both regimes, ZT results turn out to be, by far, too small for direct exploitation in thermoelectric devices, the highest achievable value being estimated in $\sim 10^{-8}$.

II. METHODS

A. Boltzmann Transport Equation and electron-phonon scattering

In order to fully clarify the importance of a meticulous calculation of electron lifetimes, properly capturing their temperature dependence, we rely on the Boltzmann transport equation (BTE), which provides a broad description of transport properties [30]. In fact, BTE provides a detailed balance of the impact and relative importance of scattering processes, resulting in the description of the time evolution of a system through the distribution function $f(\mathbf{r}, \mathbf{k}, t)$ of its charge carriers (interestingly enough, a similar result also holds for phonons). This allows to rationalize the probability of finding an electron with wave vector $\mathbf{k}$ at a position $\mathbf{r}$ and time t.

In general, in a homogeneous and isotropic conductor where nonequilibrium conditions are imposed, the Boltzmann transport equation is cast in the form [31]

$$\frac{\partial f_n(\mathbf{k},t)}{\partial t} = \mathbf{v}_\mathbf{k} \cdot \nabla_\mathbf{r} f_n(\mathbf{k},t) + \frac{\mathbf{F}}{\hbar} \cdot \nabla_\mathbf{k} f_n(\mathbf{k},t) + \left(\frac{\delta f_n(\mathbf{k},t)}{\delta t}\right)_{\text{coll}}, \quad (1)$$

where $f_n(\mathbf{k}, t)$ represents the distribution function of electrons with wave vector $\mathbf{k}$ in the nth electronic band at time t and $\mathbf{v}_\mathbf{k}$ denotes the group velocity of the carriers, subjected to the action of an external force $\mathbf{F}$ (due to an electric or a magnetic field).

The collisional term $(\delta f_n/\delta t)_{\text{coll}}$, formally cast as the time-derivative of a functional, accounts for the internal interactions occurring among the carriers. More specifically, this term models the rate at which electrons are scattered from one state to another. These events determine a redistribution of carriers in the phase space, which ultimately leads to the relaxation of the system towards the equilibrium distribution $f_0(\mathbf{k})$. This collisional term can be written, at various levels of mathematical sophistication [27], in terms of all possible initial and final states of the scattering processes, which can involve defects, impurities, phonons, or the other charge carriers [22]. A general form for the the collisional functional usually adopted [31,32] is

$$\left(\frac{\delta f(\mathbf{k},t)}{\delta t}\right)_{\text{coll}} = \sum_{\mathbf{k}'} \{W_{\mathbf{k}',\mathbf{k}} f(\mathbf{k}',t)[1 - f(\mathbf{k},t)] - W_{\mathbf{k},\mathbf{k}'} f(\mathbf{k},t)[1 - f(\mathbf{k}',t)]\}, \quad (2)$$

where $W_{\mathbf{k},\mathbf{k}'}$ is the transition rate for an electron to scatter from state $\mathbf{k}$ to state $\mathbf{k}'$, $W_{\mathbf{k}',\mathbf{k}}$ is the rate for the opposite event, and $f(\mathbf{k}, t)$ and $f(\mathbf{k}', t)$ are the occupation probabilities at time t of these states. This form reflects the balance between incoming and outgoing scattering events, with the factor $[1 - f(\mathbf{k}, t)]$ accounting for the Pauli exclusion principle, restricting electrons from scattering into already-occupied states. In general, the transition rates $W_{\mathbf{k},\mathbf{k}'}$ and $W_{\mathbf{k}',\mathbf{k}}$ can be naturally derived using time-dependent perturbation theory [22], but their actual analytical form is strictly determined by the specific nature of the scattering process considered, a problem which will be addressed next.

In a steady-state regime where a homogeneous external electric field $\mathbf{E}$ and a temperature gradient $\nabla_\mathbf{r} T$ are imposed to the system, Eq. (1) is naturally re-cast in the form [22]

$$\left(\frac{\delta f_n(\mathbf{k})}{\delta t}\right)_{\text{coll}} = -\mathbf{v}_\mathbf{k} \cdot \nabla_\mathbf{r} T \frac{\partial f_n(\mathbf{k})}{\partial T} - e\mathbf{E} \cdot \mathbf{v}_\mathbf{k} \frac{\partial f_n(\mathbf{k})}{\partial \varepsilon_{n\mathbf{k}}}, \quad (3)$$

where $\varepsilon_{n\mathbf{k}}$ represents the energy of the electron in the nth band at $\mathbf{k}$ wave vector.

To further proceed, it is necessary to work out an expression for the scattering rates, a choice naturally linked to the dominant intrinsic scattering mechanisms. In the case of perovskites, electron-phonon interaction was extensively reported to dictate the transport properties [9,33–36]. For this reason, we will only restrict to this scattering mechanism. From an atomistic perspective, electron-phonon scattering origins from the perturbation that a phonon with wave vector $\mathbf{q}$ in the ν vibrational eigenstate generates on an otherwise-fully-relaxed crystal. By labeling with $|\psi_{n\mathbf{k}}\rangle$, the wave function corresponding to an unperturbed electron state with $\mathbf{k}$ wave number in the nth band, the correction to the electronic energies when the crystal field potential V is perturbed by the presence of a phonon eigenmode $\{\mathbf{q}, \nu\}$ is proportional to [37]

$$g^{\nu}_{mn}(\mathbf{k},\mathbf{q}) = \langle \psi_{m\mathbf{k}+\mathbf{q}} | \partial_{\mathbf{q}\nu} V | \psi_{n\mathbf{k}} \rangle, \quad (4)$$

where $g^{\nu}_{mn}(\mathbf{k}, \mathbf{q})$ is referred to the electron-phonon coupling matrix, while $\partial_{\mathbf{q}\nu} V$ stands for [37]

$$\partial_{\mathbf{q}\nu} V = \sum_{p\kappa\alpha} \sqrt{\frac{\hbar}{2M_\kappa \omega_{\mathbf{q}\nu}}} e^{i\mathbf{q}\cdot\mathbf{R}_p} e_{\kappa\alpha\nu}(\mathbf{q}) \frac{\partial V}{\partial R_{p\kappa\alpha}}, \quad (5)$$

where $R_{p\kappa\alpha}$ denotes the αth Cartesian component of the equilibrium position of atom κ of mass M_κ in the pth unit cell with origin $\mathbf{R}_p$, and $e_{\kappa\alpha\nu}(\mathbf{q})$ is the αth Cartesian component of the vibrational eigenmode with frequency $\omega_{\mathbf{q}\nu}$ for atom κ. By properly defining the electron-phonon Hamiltonian [38] describing the interaction between an electron with initial momentum $\mathbf{k}$ scattering to a final state with momentum $\mathbf{k} + \mathbf{q}$

through the absorption or emission of a phonon in the $\{\mathbf{q}, \nu\}$ eigenmode, the transition rates appearing in Eq. (2) can be computed. The resulting form for the collisional functional is calculated as [37]

$$\left(\frac{\delta f_n(\mathbf{k})}{\delta t}\right)_{\text{coll}} = \frac{2\pi}{\Omega_{\text{BZ}}\hbar}\sum_{m,\nu}\int \mathrm{d}^3q\left|g^{\nu}_{mn}(\mathbf{k},\mathbf{q})\right|^2\big[f_n(\mathbf{k})(1-f_m(\mathbf{k}+\mathbf{q}))\delta\big(\Delta\varepsilon^{nm}_{\mathbf{k},\mathbf{q}}+\hbar\omega_{\mathbf{q}\nu}\big)n_\nu(\mathbf{q}) + f_n(\mathbf{k})(1-f_m(\mathbf{k}+\mathbf{q}))\delta\big(\Delta\varepsilon^{nm}_{\mathbf{k},\mathbf{q}}-\hbar\omega_{\mathbf{q}\nu}\big)(n_\nu(\mathbf{q})+1) - (1-f_n(\mathbf{k}))\,f_m(\mathbf{k}+\mathbf{q})\delta\big(-\Delta\varepsilon^{nm}_{\mathbf{k},\mathbf{q}}+\hbar\omega_{\mathbf{q}\nu}\big)n_\nu(\mathbf{q}) - (1-f_n(\mathbf{k}))\,f_m(\mathbf{k}+\mathbf{q})\delta\big(-\Delta\varepsilon^{nm}_{\mathbf{k},\mathbf{q}}-\hbar\omega_{\mathbf{q}\nu}\big)(n_\nu(\mathbf{q})+1)\big], \tag{6}$$

where $n_\nu(\mathbf{q})$ is the phonon occupation number, Ω_{BZ} is the volume of the Brillouin zone, and the short-hand notation $\Delta\varepsilon^{nm}_{\mathbf{k},\mathbf{q}} = \varepsilon_{n\mathbf{k}} - \varepsilon_{m\mathbf{k}+\mathbf{q}}$ is introduced.

Equation (6) represents the most general collisional functional for the process of emission/absorption of a phonon from/by an electron. By using this form, BTE in Eq. (3) accounts for the transport regime when electron-phonon scattering mechanisms are dominant and usually referred to as the full-BTE.

It is evident that solving the full collisional integral is quite computationally intensive due to the need to account for all possible interactions and to evaluate a large number of multi-dimensional integrals. As a result, several numerical schemes and approximations are employed to make the problem tractable, as outlined in the following.

B. Formal solution of the Boltzmann Transport Equation

In order to bypass the complexity in solving the full BTE [Eqs. (3) and (6)], a linearization procedure is commonly adopted, thus obtaining a numerical problem that can be solved iteratively.

This approach is straightforward provided that (a) no imposed temperature gradient is present and (b) a weak electric field is considered. This state of affairs corresponds to the typical experimental conditions in which transport coefficients [for example, electrical conductivity $\sigma(T)$] are measured. Under these assumptions, and by taking the derivative of both the sides of the full BTE with respect to each possible α Cartesian component of the electric field E_α, it can be shown [24] that the solution to the BTE is equivalent to solving

$$-ev^{\beta}_{n\mathbf{k}}\frac{\partial f^0_n(\mathbf{k})}{\partial\varepsilon_{n\mathbf{k}}} = \frac{1}{\Omega_{\text{BZ}}}\sum_m\int \mathrm{d}^3q \times\left[\frac{\partial_{E_\beta}f_m(\mathbf{k}+\mathbf{q})}{\tau_{m\mathbf{k}+\mathbf{q}\to n\mathbf{k}}} - \frac{\partial_{E_\beta}f_n(\mathbf{k})}{\tau_{n\mathbf{k}\to m\mathbf{k}+\mathbf{q}}}\right], \tag{7}$$

where $v^{\beta}_{n\mathbf{k}}$ is the Cartesian component of the velocity along the β direction for an electron in the nth band and $\mathbf{k}$ wave vector, and $\partial_{E_\beta}f_n(\mathbf{k}) = (\partial f_n(\mathbf{k})/\partial E_\beta)|_{\mathbf{E}=\mathbf{0}}$, quantifying to what extent the electric field affects the distribution function in a weak regime. The partial decay rates

$$\tau^{-1}_{n\mathbf{k}\to m\mathbf{k}+\mathbf{q}} = \sum_\nu\frac{2\pi}{\hbar}\left|g^{\nu}_{mn}(\mathbf{k},\mathbf{q})\right|^2 \times\big[\big(n_\nu(\mathbf{q})+1-f^0_m(\mathbf{k}+\mathbf{q})\big)\delta\big(\Delta\varepsilon^{nm}_{\mathbf{k},\mathbf{q}}-\hbar\omega_{\mathbf{q}\nu}\big) + \big(n_\nu(\mathbf{q})+f^0_m(\mathbf{k}+\mathbf{q})\big)\delta\big(\Delta\varepsilon^{nm}_{\mathbf{k},\mathbf{q}}+\hbar\omega_{\mathbf{q}\nu}\big)\big] \tag{8}$$

describe the time evolution of the population at any given electron state dictated by phonon-assisted transitions to other states. Equation (7) represents the linearized BTE (hereafter L-BTE), which can be solved without further approximations by using an iterative scheme [23].

This approach, however, is still computationally demanding because a substantial sampling of the Brillouin zone is required to accurately evaluate any term there appearing. To master the computational complexity associated with dense $\mathbf{k}$- and $\mathbf{q}$-point grids, interpolation schemes are adopted, notably including the one based on the Wannier functions [39] which allow a faster and smoother interpolation of electronic band structures and electron-phonon matrix elements over finer $\mathbf{k}$-meshes thanks to the high degree of localization in real space. This significantly reduces the computational burden compared to direct calculations on dense grids.

For further convenience, we introduce the lifetimes $\tau_{n\mathbf{k}}$ of the state $(n,\mathbf{k})$ calculated as the inverse of the sum of all scattering rates out of the state $\mathbf{k}$:

$$\tau^{-1}_{n\mathbf{k}} = \sum_m\tau^{-1}_{n\mathbf{k}\to m\mathbf{k}+\mathbf{q}} = \sum_{m,\nu}\int\frac{\mathrm{d}^3q}{\Omega_{\text{BZ}}}\left|g^{\nu}_{mn}(\mathbf{k},\mathbf{q})\right|^2 \times\big[(1-f_m(\mathbf{k}+\mathbf{q}))\delta\big(\Delta\varepsilon^{nm}_{\mathbf{k},\mathbf{q}}+\hbar\omega_{\mathbf{q}\nu}\big) + (n_\nu(\mathbf{q})+1)\delta\big(\Delta\varepsilon^{nm}_{\mathbf{k},\mathbf{q}}-\hbar\omega_{\mathbf{q}\nu}\big)\big]. \tag{9}$$

These are, in fact, the key quantities to be calculated for our investigation.

C. BTE and transport properties: Electrical conductivity and Seebeck coefficient

By expressing the electrical current $\mathbf{j}(\mathbf{E})$ in the presence of an electric field $\mathbf{E}$ as an integral on the $\mathbf{k}$-space

$$\mathbf{j}(\mathbf{E}) = -\frac{e}{(2\pi)^3}\sum_n\int\mathrm{d}^3k\,\mathbf{v}_{n\mathbf{k}}f_n(\mathbf{k})(\mathbf{E}) \tag{10}$$

the expression for the electrical conductivity tensor $\sigma_{\alpha\beta}$ is

$$\sigma_{\alpha\beta}(T) = \left.\frac{\partial j_\alpha}{\partial E_\beta}\right|_{\mathbf{E}=\mathbf{0}} = -\frac{e}{(2\pi)^3}\sum_n\int\mathrm{d}^3k\,v^{\alpha}_{n\mathbf{k}}\partial_{E_\beta}f_n(\mathbf{k}). \tag{11}$$

The Seebeck coefficient $S_{\alpha\beta}(T)$, which provides the thermoelectric voltage along the α-direction in response to a thermal

gradient applied along the β-direction, is given by:

$$S_{\alpha\beta}(T) = -\frac{1}{eT}\frac{\sum_{n,\mathbf{k}} \tau_{n\mathbf{k}} v^{\alpha}_{n\mathbf{k}} v^{\beta}_{n\mathbf{k}} (\varepsilon_{n\mathbf{k}} - \mu)\left(-\frac{\partial f^0_n(\mathbf{k})}{\partial \varepsilon_{n\mathbf{k}}}\right)}{\sum_{n,\mathbf{k}} \tau_{n\mathbf{k}} v^{\alpha}_{n\mathbf{k}} v^{\beta}_{n\mathbf{k}} \left(-\frac{\partial f^0_n(\mathbf{k})}{\partial \varepsilon_{n\mathbf{k}}}\right)}, \quad (12)$$

where T is the absolute temperature and μ is the chemical potential.

D. Numerical implementation

The present first-principles calculations for $Cs_2NaYbCl_6$ have been performed using the `Quantum ESPRESSO` suite [40,41]. The initial structure was generated and subjected to a careful relaxation to achieve the minimum energy configuration by imposing a force convergence threshold of 10^{-5} eV/Å. To solve the Kohn-Sham equations, we employed the Perdew-Burke-Ernzerhof (PBE) exchange-correlation functional [42]. The plane-wave basis set was defined with a kinetic energy cutoff of 70 Ry and a charge density cutoff of 350 Ry. Frozen-core approximation was adopted by using the ultrasoft scalar relativistic pseudopotentials from the `PSLibrary` [43]. In order to fully describe the correct electronic configuration of $Cs_2NaYbCl_6$, the trivalent state of Yb ($4f^{13}5d^1$) was described by adopting the `spdn` pseudopotential, with f electrons included in the core. The alternative choice to fully exploit all Yb valence electrons would predict a metallic behavior, in contrast with this experiment. (See the Supplementary Material [44] for our report on a comparison of `spdn` results with the corresponding ones obtained with a full f electrons treatment, including Hubbard corrections.)

A Monkhorst-Pack **k**-point mesh of $7 \times 7 \times 7$ was used to sample the Brillouin zone during the self-consistent field (SCF) calculations. In order to achieve a manageable computational cost, no spin-orbit corrections were explicitly included after first verifying that they produce a minor impact on higher (lower) states of valence (conduction) bands.

Following the SCF cycle, we refined the electronic band structure through non-self-consistent field (NSCF) calculation using a denser $15 \times 15 \times 15$ **k**-point grid. This higher resolution in reciprocal space is crucial to get accurate band structure and density of states (DOS). Next, phonon properties have been calculated in the framework of Linear Response Theory using the `ph.x` module of `Quantum ESPRESSO`, with a $7 \times 7 \times 7$ **q**-point grid.

To analyze the contributions of individual atomic species to the electronic transport properties, we also computed the projected density of states (PDOS), which have been next used to identify the atomic orbitals that significantly influence the transport characteristics. This procedure undergoes the Wannierization process described below.

`The EPW` (Electron-Phonon coupling using Wannier functions) software package [39] was used to interpolate the electron and phonon properties. We performed Wannierization on the electronic states within the energy range of 5–7 eV around the Fermi level ε_F, thus capturing all the relevant bands. Based on the PDOS analysis, we selected Cl-p orbitals as the starting projections for the Wannier functions. We adopted fine interpolation $30 \times 30 \times 30$ grids in **q**-space and $15 \times 15 \times 15$ grids in **k**-space to maintain high accuracy. The interpolated electronic bands were compared with the original results from `Quantum ESPRESSO`, showing excellent agreement (see Sec. III for the discussion).

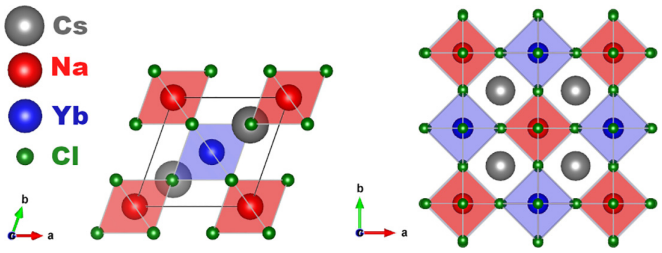

FIG. 1. Primitive (left) and conventional (right) unit cell structure of $Cs_2NaYbCl_6$ after full structural relaxation.

By using the `EPW` module, the linearized Boltzmann transport equation (BTE) was eventually solved by using the iterative approach to determine the lifetimes $\tau_{n\mathbf{k}}$ provided in Eq. (9) as functions of electronic energy. In addition, the temperature-dependent electrical mobility $\mu(T)$ for different carrier concentrations n_c were calculated, allowing to extract the electrical conductivity $\sigma(T)$ and, by adopting the `BoltzTraP2` code [45], the Seebeck coefficient was determined.

Finally, the dimensionless figure of merit ZT was computed by combining the electronic transport properties obtained from the detailed `EPW` analysis with the previously predicted [29] thermal conductivity. In particular, we remark that the thermal conductivity was calculated taking into account anharmonic contributions up to the fourth order.

III. RESULTS AND DISCUSSION

A. Electronic band structure, phonons, and electron-phonon lifetimes

The structure of the optimized primitive unit cell of $Cs_2NaYbCl_6$ is shown in Fig. 1. The calculated structural parameters reported in Table I are in excellent agreement with experimental data: the cell angles ($\alpha = \beta = \gamma = \pi/3$) are just the same as experimental observations, while the magnitudes of the three basis vectors ($a = b = c = 7.63$ Å) show discrepancies of less than 1%. A result which stands for the reliability of the adopted computational setup. The electron properties, summarized by the band structure and density of states (DOS) shown in Figs. 2 and 3, respectively, reveal the presence of a direct band gap as large as 5.3 eV and remarkably different bands for valence and conduction states. The morphology of the topmost-occupied bands indicates modest curvature, suggesting that the corresponding charge carriers have small group velocities. Accordingly, they are expected to be more localized in space (which, incidentally, indicates that they marginally contribute to conduction).

TABLE I. Lattice parameters and angles for $Cs_2NaYbCl_6$ primitive and conventional cubic cell as resulting from DFT calculations.

Parameter	Primitive	Conventional
$a = b = c$	7.63 Å	10.79 Å
$\alpha = \beta = \gamma$	60°	90°

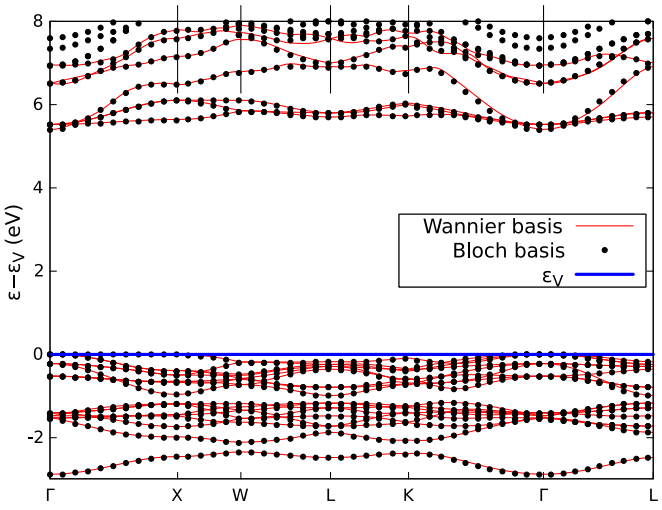

FIG. 2. Electronic band structure of $Cs_2NaYbCl_6$ calculated as Bloch states (black dots) and interpolated using Wannier functions (red lines). The zero of energy is set at the top of the valence band ε_V.

Notably, the first completely unoccupied bands do exhibit substantial curvature, indicating lower effective masses for conduction electrons, and, even if not accessible for thermally activated carriers due to the presence of a very large energy gap, still they are of valuable interest in two cases: (i) when an *n*-doping is achieved, and (ii) when the double halide perovskite is used as electron transport layer, especially in energy-harvesting applications (mainly thermoelectric and photovoltaic) or light-emitting devices (such as OLED). The numerical values of effective masses for holes in the topmost valence band and electrons in the first two conduction bands are reported in Table II, as obtained by parabolic fitting along ΓK, ΓX, and ΓL directions. The results display a sizable difference between the behavior of the charge carriers, suggesting (as we will demonstrate in the following sections) that electrons are likely to show higher mobility.

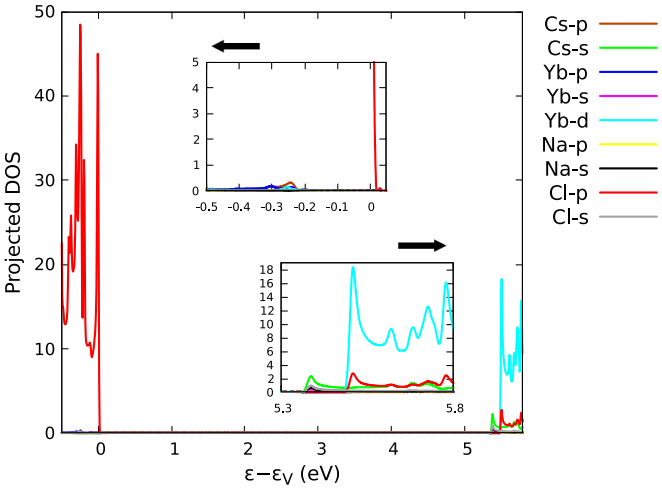

FIG. 3. Projected density of states (PDOS) highlighting the contributions of Cs, Na, Yb, and Cl orbitals.

TABLE II. Effective masses m^* of electrons and holes along different crystallographic directions. Values are reported in electron rest mass m_0 units.

Carrier	m^*(ΓK)	m^*(ΓX)	m^*(ΓL)
Heavy hole	5.82	50.8	1.75
Light hole 1	2.82	2.00	2.95
Light hole 2	2.06	2.00	2.95
Electron 1st CB	0.61	0.61	12.50
Electron 2nd CB	3.17	8.47	3.10
Electron 2nd CB	2.17	1.62	4.00
Electron 2nd CB	1.49	1.62	4.00

In order to better elucidate the physical origin of these features, the electronic structure has been further analyzed through the study of the projected density of states (PDOS) onto atomic orbitals. Figure 3 highlights the predominant role of the halogen (Cl) *p*-orbitals in the valence bands, while the conduction bands are dominated by the contribution of Cs-*s* and Yb-*d* orbitals, with the halogen playing a marginal role in this case. Following this observation, we concluded that no bands with mixed atomic orbital nature are present in the valence states, while such mixing is possible in conduction states. Thus, the Wannierization procedure was carried out just using Cl orbitals as projectors for valence states and Cs-*s* and Yb-*d* orbitals for conduction states. A sufficiently wide energy window (2.5 eV) was set to include all contributing electronic states possibly accessible. To verify the accuracy of the Wannierization procedure, Fig. 2 shows the interpolated electronic bands (red lines) superimposed on those directly obtained from `Quantum ESPRESSO` calculations (black points). The agreement indicates that the interpolation guess and the chosen density of **k**-points are accurate enough to proceed with the calculation of electron-phonon scattering rates.

The above computational setup has also been used to calculate the phonon dispersion curves in linear response (reported in Fig. 4 and in agreement with our previous study [29], where finite-displacements were used). We observe the presence of three distinct regions, depending on the phonon energies and character: a low- (high-) energy region, (light red and blue, respectively) where only acoustic (optical) phonons are present, and a very narrow but distinct region (purple) where both are present. This partitioning will be useful in the following for characterizing the electron-phonon scattering. By eventually calculating the electron-phonon matrix elements given in Eq. 4 and iteratively solving the linearized BTE, we were able to proceed with the determination of the energy-resolved carrier lifetimes [given in Eq. (9)] at different temperatures, both in the hole and electron transport regime shown in Fig. 5(a) and Fig. 5(b), respectively. We focused on the very broad temperature range $100 \leqslant T \leqslant 800$ K nevertheless restricting to a range where $Cs_2NaYbCl_6$ was experimentally found to be stable [29]. In the following, we will refer to $\tau^h_{n\mathbf{k}}$ and $\tau^e_{n\mathbf{k}}$ for the lifetimes calculated for carriers relative to valence and conduction states, respectively. In both cases, Eq. (9) was used.

In Fig. 5(a), the magnitude of the mode- and energy-resolved lifetime for holes $\tau^h_{n\mathbf{k}}$ is shown as a function of the

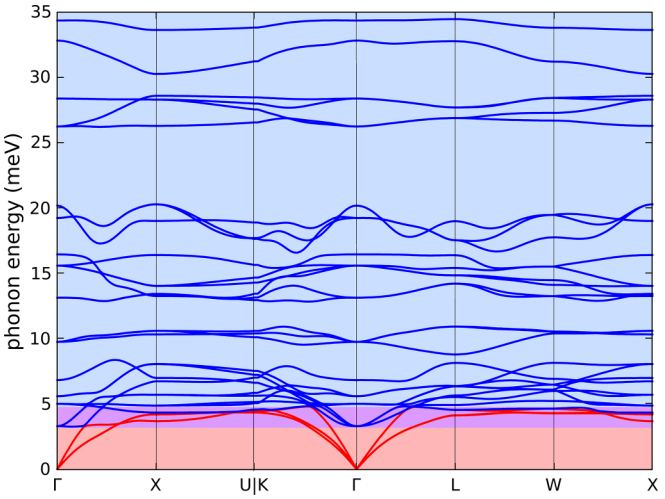

FIG. 4. Phonon dispersion curves of $Cs_2NaYbCl_6$: red and blue lines indicate acoustic and optical phonons, respectively. The background color is a visual indication of the energy range where acoustic (light red) and optical (light blue) phonons are dominant in scattering electrons. In the violet energy range, acoustic and optical modes equally contribute.

energy ε. It is found that, at any energy, lifetimes monotonically decrease as the temperature T is increased, a trend expected by the overall increase of the number of phonons available to trigger scattering events. However, at any fixed T, a more complex behavior is actually observed. In fact, states at the top of the valence band show lifetimes as high as 7 fs (at 100 K), while a sudden drop is observed, reducing the lifetimes to an average ∼2 fs value for electronic states lying at energies $\varepsilon - \varepsilon_V < 50$ meV. This is a clear indication that, at any temperature, long lifetimes are possible only for a very few electronic states around ε_V.

The magnitude of the mode- and energy-resolved lifetime for electrons $\tau^e_{n\mathbf{k}}$ is shown in Fig. 5(b) as a function of energy ε. Overall, the electron lifetimes at a fixed energy decrease monotonically as the temperature T is increased. This aligns with the behavior observed for valence bands and we link it to the higher population of phonons participating to the scattering processes. However, the detailed behavior of $\tau^e_{n\mathbf{k}}$ as a function of energy and temperature exhibits some quantitative differences from the case of holes, which is worth to describe more carefully. At low temperatures (100 K), electrons at the conduction band minimum show lifetimes at least one order of magnitude larger as compared to the topmost valence bands, specifically reaching a value of ∼800 fs. This indicates that low energy carriers are subject to a consistently weaker scattering.

In order to demonstrate the difference in the scattering for, respectively, holes and electrons, in Fig. 6 we report the electron-phonon coupling strength g^{ν}_{mn} in the case of holes in the highest valence band [Fig. 6(a)] and electrons in the lowest conduction band [Fig. 6(b)], in both cases resolved for each individual phonon branch. Only intra-band interactions (i.e., $m = n$) are taken into account, thus focusing on the precise behavior of the highest valence band and the lowest conduction band. It is evident from Fig. 6 that the intrinsic strength of electron-phonon interaction is significantly lower (approximately two order of magnitude) in the case of an electron transport regime. We will show that this fact, combined with the distinct difference in the effective masses of the carriers, will generate a higher value of mobility for electrons compared to holes.We also remark that while both types of carriers experience a decrease in lifetime as the temperature rises, the distribution of $\tau_{n\mathbf{k}}$ over the energy range appears broader for electrons than for holes. In fact, by varying energy ε, electron lifetimes experience a two order of magnitude variation in the case of electrons and one order of magnitude in the case of holes. This broader distribution, again, likely results from the different nature of the conduction band states compared to the valence band states.

In order to better elucidate the key differences discussed so far, we now focus on the spectral decomposition of the scattering rates $\tau^{-1}_{n\mathbf{k}}$ as a function of the energy $\varepsilon_{\mathrm{ph}}$ of the phonons involved in scattering processes, following the definition used in Refs. [46,47]. The analysis, carried out for both

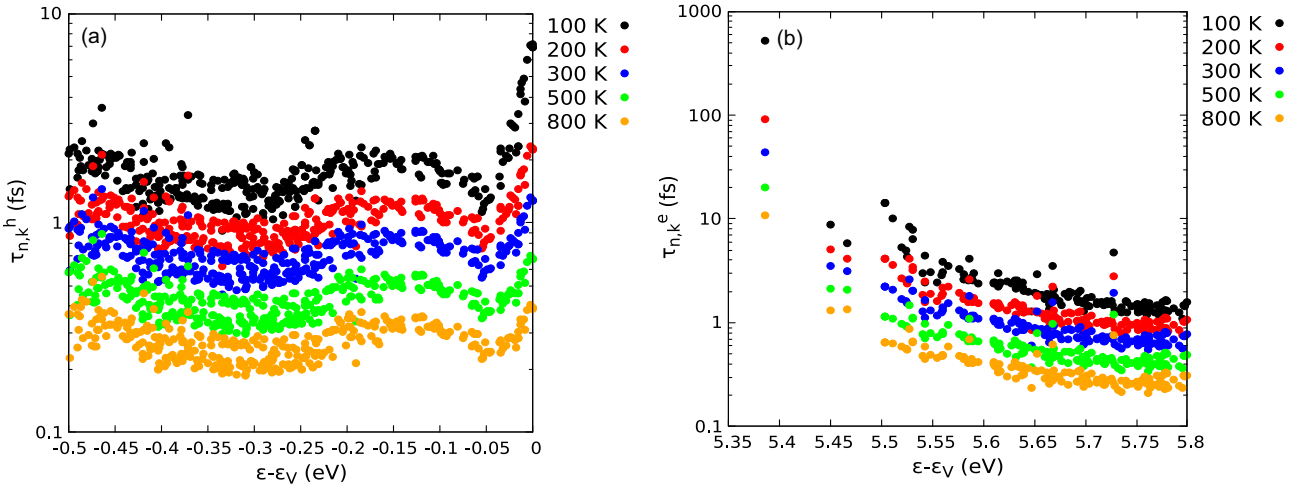

FIG. 5. Hole (a) and electron (b) lifetimes as a function of Kohn-Sham state energy and temperature in $Cs_2NaYbCl_6$. The top of the highest valence band ε_V is set to zero as reference.

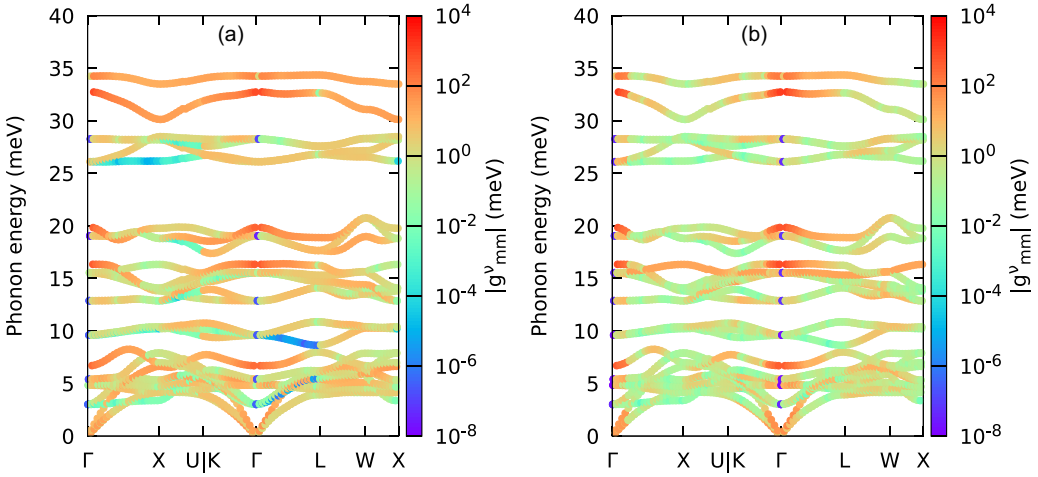

FIG. 6. (a) Electron-phonon coupling strength $|g^{\nu}_{mn}|$ in the case of holes in the highest valence band and (b) electrons in the lowest conduction band, resolved for each individual phonon branch. Only intraband interactions (i.e., $m = n$) are taken into account.

holes- and electron-mediated regimes, allows us to investigate the relative contribution, at any given T, of acoustic and optical phonons in determining the carrier lifetimes observed in Fig. 5.

The spectral scattering rate density for holes (h-SSRD) and electrons (e-SSRD) as a function of phonon energy is shown in Figs. 7(a) and 7(b), respectively. In both the cases, at all the investigated temperatures, the SSRDs extend on the entire phonon spectrum and exhibit three main peaks at ∼6, 17, and 32 meV, which we attribute to scattering events, respectively involving acoustic (first peak) or optical (second and third peak) phonons. Focusing on the intensities, we observe a striking difference between holes and electrons: h-SSRD intensities are, in fact, four times larger than the corresponding e-SSRD, which proofs the dominant role of hole scattering.

To complete our analysis, we analyzed the integral of the SSRD over the entire phonon energy spectrum, i.e. the cumulative scattering rate $\tau^{-1}_{j,\mathrm{cum}}$ for holes ($j = h$) and electrons ($j = e$). $\tau^{-1}_{h,\mathrm{cum}}$ as a function of phonon energy is shown in Fig. 8(a) at two distinct temperatures, namely 100 K and 800 K. The cumulative behavior clearly reveals how the impact of different phonon modes, previously examined by using the SSRD, contribute to the overall scattering processes in the material. At 100 K, the cumulative curve grows as phonon energy increases, reaching a maximum value around 30 fs^{-1} at the highest phonon energy (35 meV). The contribution from lower-energy phonons (up to 10 meV) is significant and accounts for about 1/3 of the overall value of the scattering rate. At 800 K, the magnitude of the cumulative scattering rate is much higher, reaching approximately 50 fs^{-1} at 40 meV. Higher-energy phonons (especially optical phonons in the range of 25–40 meV) contribute significantly to the scattering processes at this temperature. This observation correlates with our earlier analysis, where optical phonons were found to play a major role in determining much shorter lifetimes.

The cumulative scattering rate $\tau^{-1}_{e,\mathrm{cum}}$ for electrons [Fig. 8(b)] at 100 K and 800 K shows some notable differences. At 100 K, it steadily grows with phonon energy,

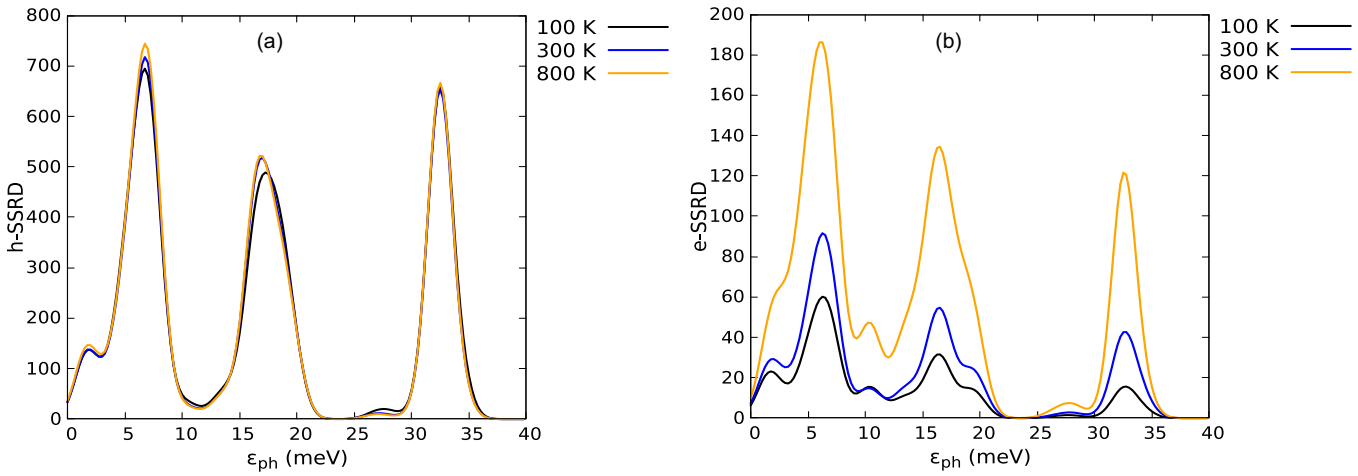

FIG. 7. (a) Spectral scattering rates density for holes (h-SSRD) and (b) electrons (e-SSRD) resulting from electron-phonon scattering events as a function of the energy of the involved phonon and the temperature of the system.

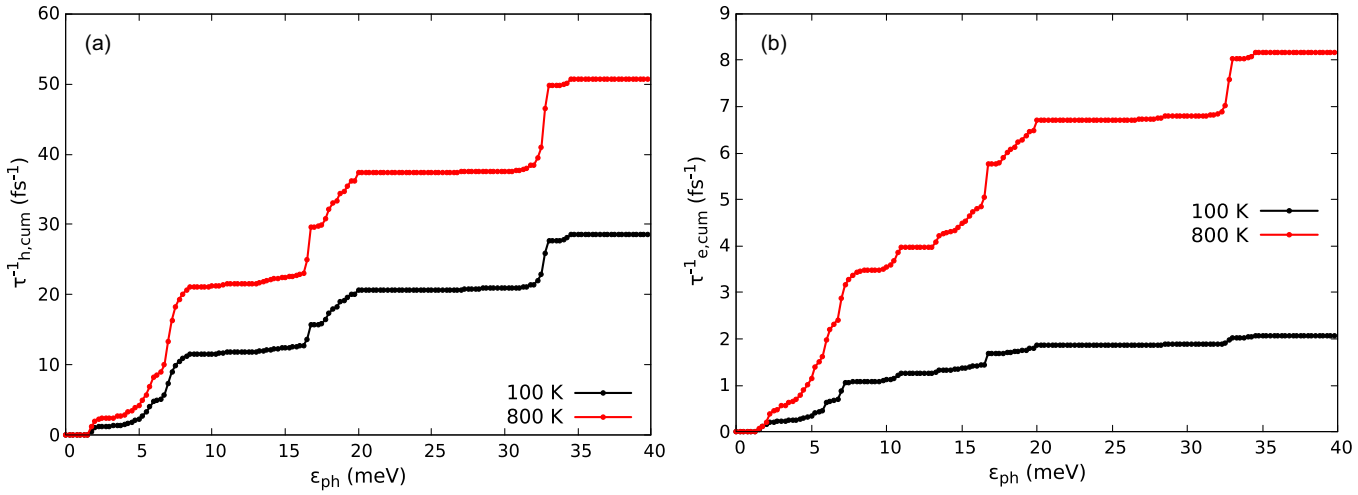

FIG. 8. (a) Cumulative scattering rate for holes and (b) electrons resulting from electron-phonon scattering events as a function of the energy of the phonon involved and the temperature of the system.

reaching a maximum of about 2 fs^{-1} at 40 meV. This is a direct consequence of the broader profile of the corresponding spectral decomposition, allowing the contribution of a larger number of phonon modes to the scattering rate. At 800 K, the cumulative inverse lifetime increases much more rapidly, reaching nearly 8 fs^{-1} at 40 meV. However, the magnitude of $\tau^{-1}_{e,\mathrm{cum}}$ is significantly lower than that for holes. This suggests that, while optical phonons dominate the scattering processes at higher temperatures for both electrons and holes, the overall coupling between electrons and phonons is weaker compared to holes.

B. Mobilities and Seebeck coefficient

In Sec. III A, we thoroughly analyzed the electron and holes lifetimes resulting from the electron-phonon scattering processes. In this subsection, we now focus on their role in determining intrinsic mobility $\mu(T)$ and the Seebeck coefficient $S(T)$ for $300\,\mathrm{K} \leqslant T \leqslant 800\,\mathrm{K}$. More specifically, we referred to Eqs. (11) and (13) for the calculation of $\sigma_{\alpha\beta}(T)$ and $S_{\alpha\beta}(T)$, respectively, with the mobility defined as $\mu_{\alpha\beta}(T) = \sigma_{\alpha\beta}/|e|n_c$, with n_c the concentration of intrinsic carriers. From our direct calculations, we observed that only the diagonal components were nonzero and equal, indicating that the transport coefficients are isotropic. Accordingly, we defined $\mu(T)$ and $S(T)$ as the $\alpha\beta = 11$ component.

By using the EPW transport module, we evaluated mobility $\mu(T)$ for a concentration of carriers $n_c = 10^{11}\,\mathrm{cm}^3$, the typical value expected in a realistic defect-free sample [48]. The results for electrons (red) and holes (blue) are shown in Fig. 9. As expected, longer lifetimes of electrons compared to holes result in electron mobilities significantly higher; focusing on $T = 300\,\mathrm{K}$, in fact, electron mobility reaches a value of $10\,\mathrm{cm}^2\mathrm{V}^{-1}\mathrm{s}^{-1}$, while hole mobility is one order of magnitude lower ($0.7\,\mathrm{cm}^2\mathrm{V}^{-1}\mathrm{s}^{-1}$). When comparing our results with the corresponding mobilities obtained for another DHP, namely $Cs_2AgBiCl_6$ [9] where at $T = 300\,\mathrm{K}$, $\mu_e = 7.1\,\mathrm{cm}^2\,\mathrm{V}^{-1}\mathrm{s}^{-1}$ and $\mu_h = 9.4\,\mathrm{cm}^2\,\mathrm{V}^{-1}\mathrm{s}^{-1}$ are reported, we observe not only a difference of one order of magnitude in μ_h, but also a distinct trend. Unlike $Cs_2AgBiCl_6$, where holes exhibit higher mobility, in $Cs_2NaYbCl_6$, electrons in fact, also show higher mobility. We argue that such difference stems from the substitution of the constituting B_1, B_2 cations. This produces very distinctive differences in both phonon dispersion curves as well as electronic band-structure. In particular, by comparing the effective masses obtained for $Cs_2NaYbCl_6$ perovskite and the one investigated in Ref. [9], holes appear more massive, a fact which contributes to the lower mobility values and highlights the need to evaluate for each DHP the correct lifetime, which seems poorly transferable. We also notice, from Fig. 9, that both mobilities exhibit an exponential decay for increasing temperature, again in agreement with the observed reduction of the lifetimes. Interestingly enough, the different decay rate of hole and electron mobilities can be straightforwardly interpreted as a consequence of the different behavior of lifetimes at increasing T. In fact, as we observe from Figs. 8(a) and 8(b), the increase of τ_h^{-1} with temperature is less pronounced compared to τ_e^{-1}. As a result, the decay of electron mobility with T is faster than the

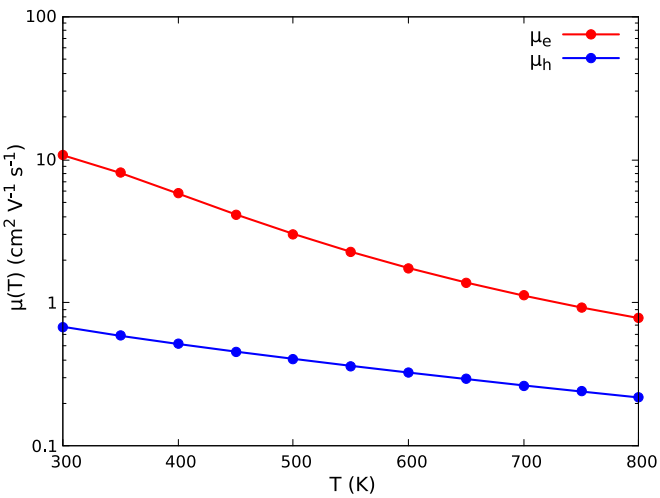

FIG. 9. Intrinsic electron (red) and hole (blue) mobilities as a function of the temperature T.

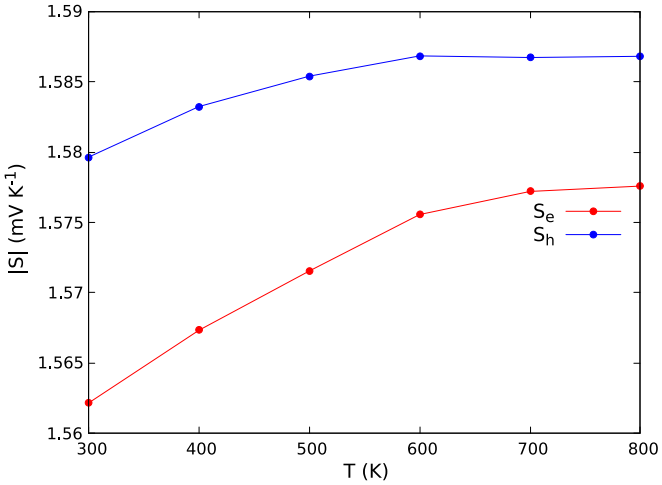

FIG. 10. Seebeck coefficient $S(T)$ for electrons (red) and holes (blue) as a function of the temperature.

corresponding decrease for holes. Finally, we observe that the typical values for electrical conductivity σ at 300 K results in $1.6 \cdot 10^{-7}\,\Omega^{-1}\,\mathrm{cm}^{-1}$ in the case of electrons, while in the case of hole-mediated conduction the values are an order of magnitude lower.

The Seebeck coefficient, by contrast, exhibits a completely opposite trend. As shown in Fig. 10 for holes (blue) and electrons (red), the values are quite similar (the largest difference, at 300 K, being of about 1%), and both increasing with T. Interestingly enough, values around 1.57–1.58 $\mathrm{mV\,K^{-1}}$ are significantly higher than the typical range $(10 - 900\,\mu\mathrm{V/K})$ [5–8,12,13,15,17–20] reported for other DHPs. This is reasonable as the Seebeck coefficient S in semiconductors is expected to increase with bandgap [49,50]. Since the Seebeck coefficient is nearly the same for both holes and electrons, while the mobility differs significantly, $Cs_2NaYbCl_6$ is expected to be more suitable for n-type doping.

C. Thermoelectric figure-of-merit *ZT*

Since electron and hole transport regimes show significant differences, as explained in Sec. III B, it is interesting to compare for each case the thermoelectric figure-of-merit, defined as

$$ZT = \frac{\sigma S^2}{\kappa_l + \kappa_e} T, \tag{13}$$

where κ_l and κ_e are the lattice and electronic contribution to thermal conductivity, respectively. In the case of $Cs_2NaYbCl_6$, the electronic contribution is totally negligible. To support this observation, we remark that we previously demonstrated [29] that modeling κ_l in the framework of Self-Consistent Phonon Theory is sufficient to reproduce experimental data. To further verify this assumption, we checked the value of κ_e, finding them negligible compared to the experimental κ values (for $300\,\mathrm{K} \leqslant T \leqslant 800\,\mathrm{K}$), which lies between 0.45 and 0.55 $\mathrm{Wm^{-1}K^{-1}}$ [29]. We, thus, calculated ZT by using only the lattice thermal conductivity.

In the case of electron- and hole-mediated transport, ZT is quite low, being of the order of 10^{-8}. More specifically, the case of electrons is in the order of $1.4 \cdot 10^{-8}$ at $T = 500\,K$, while in the case of holes the corresponding value is $0.2 \cdot 10^{-8}$, a subtle signature of the lower hole mobility.

IV. CONCLUSIONS

In this study, we performed a detailed computational analysis of the electronic structure and carrier dynamics in $Cs_2NaYbCl_6$ using a combination of Density Functional Theory (DFT) and the electron-phonon Wannier interpolation method. Our results confirm the insulating nature of the compound with a large direct band gap of 5.3 eV. The band structure and projected density of states (PDOS) analysis reveals the dominance of Cl-p orbitals in the valence band, and the contributions of Cs-p and Yb-d orbitals in the conduction band.

The electron-phonon coupling was further explored, showing significant temperature dependence for both electrons and holes. In the entire temperature range explored, $100\,\mathrm{K} \leqslant T \leqslant 800\,\mathrm{K}$, we found that for both holes and electrons, the scattering is dominated by optical phonons, but with very different magnitude. In fact, while at room temperature, the lifetimes for electrons in the lowest conduction band are approximately 40 fs, holes in the highest- occupied band display values of 1 fs, a difference of one order of magnitude.

This difference naturally reflects on the values of mobilities of the charge carriers, and reveals a clear superior conductive behavior in electron-mediated regime. Interestingly, while electron mobility is essentially in line with the values reported for a similar DHP ($Cs_2AgBiCl_6$ [9]), in the case of holes mobility we obtained $\mu_h = 0.7\,\mathrm{cm^2V^{-1}s^{-1}}$, while in $Cs_2AgBiCl_6$ is $\mu_h = 9.4\,\mathrm{cm^2V^{-1}s^{-1}}$. We argue that this difference is reasonably explained by the different environment in which Cl atoms, the major contributors to valence bands, are embedded, i.e., the difference between $B_{1,2}$ metal cations in the DHPs.

While the Seebeck coefficient of $Cs_2NaYbCl_6$ achieves relatively high values compared to other DHPs [5–8,12,13,15,17–20], we found that overall ZT are somewhat low, due to the very low intrinsic carrier concentrations. Since this effect is mainly due to the wide gap of the material, a possible strategy to increase ZT value is to engineer the material by chemical substitution of the $B_{1,2}$ metal cations or introduce dopants in order to increase carrier concentrations and, possibly, reduce the lattice thermal contribution.

ACKNOWLEDGMENTS

We acknowledge financial support under the National Recovery and Resilience Plan (NRRP), Mission 4 Component 2 Investment 1.3 - Call for Tender No. 341, published on March 13, 2022 by the Italian Ministry of University and Research (MUR) funded by the European Union – NextGenerationEU Award No.: Project code PE00000021, Concession Decree No. 1561, adopted on October 11, 2022 by the Italian Ministry of University and Research (MUR), CUP F53C22000770007, Project title: "NEST - Network 4 Energy Sustainable Transition".

[1] H. Lei, D. Hardy, and F. Gao, Lead-free double perovskite $Cs_2AgBiBr_6$: Fundamentals, applications, and perspectives, Adv. Funct. Mater. **31**, 2105898 (2021).

[2] E. T. McClure, M. R. Ball, W. Windl, and P. M. Woodward, Cs_2AgBiX_6 (X = Br, Cl): New visible light absorbing, lead-free halide perovskite semiconductors, Chem. Mater. **28**, 1348 (2016).

[3] A. E. Maughan, A. M. Ganose, M. M. Bordelon, E. M. Miller, D. O. Scanlon, and J. R. Neilson, Defect tolerance to intolerance in the vacancy-ordered double perovskite semiconductors Cs_2SnI_6 and Cs_2TeI_6, J. Am. Chem. Soc. **138**, 8453 (2016).

[4] D. Meggiolaro and F. D. Angelis, First-principles modeling of defects in lead halide perovskites: Best practices and open issues, ACS Energy Lett. **3**, 2206 (2018).

[5] L. Yan, L. Zhao, C. Zhao, and S. Lin, Theoretical understanding of thermoelectric energy conversion efficiency in lead-free halide double perovskites showing intrinsic defect tolerance, Appl. Therm. Eng. **215**, 119024 (2022).

[6] J. Liu, G. Tang, J. Zhou, and J. Hong, Two-dimensional electronic structure for high thermoelectric performance in halide perovskite $Cs_2Au(i)Au(iii)I_6$, Phys. Chem. Chem. Phys. **24**, 24975 (2022).

[7] R. Zafar, S. Naseem, S. Riaz, N. A. Noor, A. Mahmood, and K. Shahzad, Dft calculations of optoelectronic and thermoelectric properties of K_2NaTlX_6 (X = Cl, Br, I) halide double perovskites for energy harvesting applications, Phys. Scr. **98**, 115914 (2023).

[8] G. Mustafa, A. Slam, S. Saba, N. A. Noor, M. W. Iqbal, and A. Dahshan, Optoelectronic and thermoelectric characteristics of halide based double perovskites K_2YAgX_6 (X = Br, I) for energy storage applications, Polyhedron **229**, 116184 (2022).

[9] J. Leveillee, G. Volonakis, and F. Giustino, Phonon-limited mobility and electron–phonon coupling in lead-free halide double perovskites, J. Phys. Chem. Lett. **12**, 4474 (2021).

[10] V.-A. Ha, G. Volonakis, H. Lee, M. Zacharias, and F. Giustino, Quasiparticle band structure and phonon-induced band gap renormalization of the lead-free halide double perovskite $Cs_2InAgCl_6$, J. Phys. Chem. C **125**, 21689 (2021).

[11] M. Zacharias, G. Volonakis, F. Giustino, and J. Even, Anharmonic electron-phonon coupling in ultrasoft and locally disordered perovskites, npj Comput. Mater. **9**, 153 (2023).

[12] S. Niaz, M. A. Khan, N. A. Noor, H. Ullah, and R. Neffati, Bandgap tuning and thermoelectric characteristics of Sc-based double halide perovskites K_2ScAgZ_6 (Z = Cl, Br, I) for solar cells applications, J. Phys. Chem. Solids **174**, 111115 (2023).

[13] S. Charef, A. Assali, and A. Boukortt, Optoelectronic and thermoelectric properties of novel double halide perovskites Na_2AgAsX_6 (X = Cl, Br) for efficient green solar cells, Mater. Today Commun. **38**, 108065 (2024).

[14] E. Haque and M. A. Hossain, Electronic, phonon transport and thermoelectric properties of $Cs_2InAgCl_6$ from first-principles study, Comput. Condens. Matter **19**, e00374 (2019).

[15] S. Haid, W. Benstaali, A. Abbad, B. Bouadjemi, S. Bentata, and Z. Aziz, Thermoelectric, structural, optoelectronic and magnetic properties of double perovskite Sr_2CrTaO_6: First principle study, Mater. Sci. Eng., B **245**, 68 (2019).

[16] M. A. Haque, S. Kee, D. R. Villalva, W.-L. Ong, and D. Baran, Halide perovskites: thermal transport and prospects for thermoelectricity, Adv. Sci. **7**, 1903389 (2020).

[17] F. Elfatouaki, O. Farkad, R. Takassa, S. Hassine, O. Choukri, A. Ouahdani, E. A. Ibnouelghazi, D. Abouelaoualim, and A. Outzourhit, Optoelectronic and thermoelectric properties of double halide perovskite Cs_2AgBiI_6 for renewable energy devices, Solar Energy **260**, 1 (2023).

[18] S. A. Khandy and D. C. Gupta, New isostructural halide double perovskites Cs_2GeNiX_6 (X = Cl, Br) for semiconductor spintronics and thermoelectric advancements, J. Solid State Chem. **300**, 122196 (2021).

[19] N. A. Kattan, Q. Mahmood, G. Nazir, A. Rehman, N. Sfina, M. M. Al-anazy, S. A. Sofi, M. Morsi, and M. A. Amin, Modifying electronic bandgap by halide ions substitution to investigate double perovskites Rb_2AgInX_6 (X = Cl, Br, I) for solar cells applications and thermoelectric characteristics, Mater. Today Commun. **34**, 105166 (2023).

[20] S. Kumari, P. K. Kamlesh, L. Kumari, S. Kumar, S. Kumari, R. Singh, R. Gupta, M. S. Chauhan, U. Rani, and A. S. Verma, Progress in theoretical study of lead-free halide double perovskite Na_2AgSbX_6 (X = F, Cl, Br, and I) thermoelectric materials, J. Mol. Model. **29**, 195 (2023).

[21] J. He and T. M. Tritt, Recent advances in thermoelectric materials, Science **357**, eaak9997 (2017).

[22] M. Lundstrom, Fundamentals of carrier transport, 2nd edn, Meas. Sci. Technol. **13**, 230 (2002).

[23] L. A. Muscarella and E. M. Hutter, Halide double-perovskite semiconductors beyond photovoltaics, ACS Energy Lett. **7**, 2128 (2022).

[24] S. Poncé, E. R. Margine, and F. Giustino, Towards predictive many-body calculations of phonon-limited carrier mobilities in semiconductors, Phys. Rev. B **97**, 121201(R) (2018).

[25] C. Verdi and F. Giustino, Frohlich electron-phonon vertex from first principles, Phys. Rev. Lett. **115**, 176401 (2015).

[26] R. Claes, S. Poncé, G.-M. Rignanese, and G. Hautier, Phonon-limited electronic transport through first principles, Nat. Rev. Phys. **7**, 73 (2025).

[27] F. Giustino, M. L. Cohen, and S. G. Louie, Electron-phonon interaction using Wannier functions, Phys. Rev. B **76**, 165108 (2007).

[28] A. A. Mostofi, J. R. Yates, G. Pizzi, Y.-S. Lee, I. Souza, D. Vanderbilt, and N. Marzari, An updated version of wannier90: A tool for obtaining maximally-localised wannier functions, Comput. Phys. Commun. **185**, 2309 (2014).

[29] A. Cappai, C. Melis, D. Marongiu, F. Quochi, M. Saba, F. Congiu, Y. He, T. J. Slade, M. G. Kanatzidis, and L. Colombo, Strong anharmonicity at the origin of anomalous thermal conductivity in double perovskite $Cs_2NaYbCl_6$, Adv. Sci. **11**, 2305861 (2024).

[30] S. Harris, *An Introduction to the Theory of the Boltzmann Equation* (Dover Publications, 2004).

[31] J. M. Ziman,*Electrons and Phonons: The Theory of Transport Phenomena in Solids* (Oxford University Press, New York, 1960).

[32] M. Fiorentini and N. Bonini, Thermoelectric coefficients of *n*-doped silicon from first principles via the solution of the Boltzmann transport equation, Phys. Rev. B **94**, 085204 (2016).

[33] J.-J. Zhou, O. Hellman, and M. Bernardi, Electron-phonon scattering in the presence of soft modes and electron mobility in $SrTiO_3$ perovskite from first principles, Phys. Rev. Lett. **121**, 226603 (2018).

[34] Y. Yamada and Y. Kanemitsu, Electron-phonon interactions in halide perovskites, NPG Asia Mater. **14**, 48 (2022).

[35] M. Karakus, S. A. Jensen, F. D'Angelo, D. Turchinovich, M. Bonn, and E. Canovas, Phonon-electron scattering limits free charge mobility in methylammonium lead iodide perovskites, J. Phys. Chem. Lett. **6**, 4991 (2015).

[36] J. A. Steele, P. Puech, M. Keshavarz, R. Yang, S. Banerjee, E. Debroye, C. W. Kim, H. Yuan, N. H. Heo, J. Vanacken, A. Walsh, J. Hofkens, and M. B. J. Roeffaers, Giant electron–phonon coupling and deep conduction band resonance in metal halide double perovskite, ACS Nano **12**, 8081 (2018).

[37] S. Poncé, W. Li, S. Reichardt, and F. Giustino, First-principles calculations of charge carrier mobility and conductivity in bulk semiconductors and two-dimensional materials, Rep. Prog. Phys. **83**, 036501 (2020).

[38] F. Giustino, Electron-phonon interactions from first principles, Rev. Mod. Phys. **89**, 015003 (2017).

[39] S. Poncé, E. R. Margine, C. Verdi, and F. Giustino, EPW: Electron–phonon coupling, transport and superconducting properties using maximally localized Wannier functions, Comput. Phys. Commun. **209**, 116 (2016).

[40] P. Giannozzi Jr., O. Andreussi, T. Brumme, O. Bunau, M. B. Nardelli, M. Calandra, R. Car, C. Cavazzoni, D. Ceresoli, M. Cococcioni, N. Colonna, I. Carnimeo, A. D. Corso, S. de Gironcoli, P. Delugas, R. A. DiStasio Jr., A. Ferretti, A. Floris, G. Fratesi, G. Fugallo *et al.*, Advanced capabilities for materials modelling with QUANTUM ESPRESSO, J. Phys.: Condens. Matter **29**, 465901 (2017).

[41] P. Giannozzi, S. Baroni, N. Bonini, M. Calandra, R. Car, C. Cavazzoni, D. Ceresoli, G. L. Chiarotti, M. Cococcioni, I. Dabo, A. D. Corso, S. de Gironcoli, S. Fabris, G. Fratesi, R. Gebauer, U. Gerstmann, C. Gougoussis, A. Kokalj, M. Lazzeri, L. Martin-Samos *et al.*, QUANTUM ESPRESSO: A modular and open-source software project for quantum simulations of materials, J. Phys.: Condens. Matter **21**, 395502 (2009).

[42] J. P. Perdew, K. Burke, and M. Ernzerhof, Generalized gradient approximation made simple, Phys. Rev. Lett. **77**, 3865 (1996).

[43] A. Dal Corso, Pseudopotentials periodic table: From H to Pu, Comput. Mater. Sci. **95**, 337 (2014).

[44] See Supplemental Material at http://link.aps.org/supplemental/10.1103/PhysRevMaterials.9.054605 for the investigation of the role of explicit Yb f-electrons, spin-orbit coupling, and Hubbard corrections in determining the electronic structure and transport properties.

[45] G. K. H. Madsen, J. Carrete, and M. J. Verstraete, BoltzTraP2, a program for interpolating band structures and calculating semi-classical transport coefficients, Comput. Phys. Commun. **231**, 140 (2018).

[46] S. Poncé, M. Schlipf, and F. Giustino, Origin of low carrier mobilities in halide perovskites, ACS Energy Lett. **4**, 456 (2019).

[47] S. Poncé, F. Macheda, E. R. Margine, N. Marzari, N. Bonini, and F. Giustino, First-principles predictions of Hall and drift mobilities in semiconductors, Phys. Rev. Res. **3**, 043022 (2021).

[48] J. Leveillee, X. Zhang, E. Kioupakis, and F. Giustino, *Ab initio* calculation of carrier mobility in semiconductors including ionized-impurity scattering, Phys. Rev. B **107**, 125207 (2023).

[49] A. L. Kutepov and A. Ruth, Electronic structure and thermoelectric properties of CoAsSb with post-DFT approaches, Appl. Phys. A **126**, 137 (2020).

[50] H. J. Goldsmid and J. W. Sharp, Estimation of the thermal band gap of a semiconductor from seebeck measurements, J. Electron. Mater. **28**, 869 (1999).